Planetary-Scale Baroclinic Instability and the MJO

DAVID M. STRAUS

Center for Ocean–Land–Atmosphere Studies, Calverton, Maryland

RICHARD S. LINDZEN

Department of Earth, Atmosphere and Planetary Sciences, Massachusetts Institute of Technology, Cambridge, Massachusetts

(Manuscript received 8 March 1999, in final form 6 December 1999)

ABSTRACT

Eastward propagating planetary waves of zonal wavenumber one in the zonal wind (u) with phase speeds in the range of 1–10 m s^{-1}, and also with frequencies in the 30–60-day range, are studied using 39 boreal winter (austral summer) seasons (each of length 180 days) from the reanalyses of the National Centers for Environmental Prediction. The purpose of the paper is to study the relationship between these low phase speed waves in the extratropics (which are candidates for instabilities) and the low-frequency tropical waves associated with the Madden–Julian oscillation (MJO).

Planetary waves dominate the zonal wavenumber spectrum of all (eastward plus westward) transient fluctuations with phase speeds of 1–10 m s^{-1} at upper levels.

Using the theory of Y. Hayashi to separate out standing oscillations, it is found that eastward propagating waves for zonal wavenumber one have variance maxima at 63°N, 32°N, 13°N, 32°S, and 52°S at upper levels. As a percentage of the total variance for phase speeds 1–10 m s^{-1} and zonal wavenumber one, the eastward propagating waves have strong maxima at 200 hPa in the Tropics (13°N, 13°S) and at lower levels at 13°S (indicative of the MJO). The standing wave variance is maximum in northern midlatitudes. The eastward propagating wave variance for zonal wavenumber two has similar properties.

For zonal wavenumber one, eastward propagating waves at 52°N and 300 hPa are highly coherent with mid- and upper-level waves at 32°N, with a nearly perfectly out-of-phase relationship. For a base point at 32°N, 200 hPa, we find a strong coherence maximum for phase speeds of 1–10 m s^{-1} (coherence squared greater than 0.7) with upper levels in the Tropics (13°N), accompanied by a 180° relative phase shift. Coherence and phase plots with a base point at 13°N and 200 hPa show not only strong coherence with waves at 32°N, but also with waves at 13°S at 700 hPa. While results for the MJO averaging (corresponding to periods of 30–60 days) are generally similar, there is in addition a strong cross-equatorial coherence between fluctuations at 13°N and 13°S at 200 hPa, and stronger coherence with the lower tropical troposphere. The strong coherence between waves in the subtropics (32°N) and the Tropics (13°N) indicates a potential role for dynamical instability in the organization of the MJO.

Coherence and phase diagnostics for base points in the Southern Hemisphere have generally the same character, although the subtropical–tropical coherence is less dramatic (but still significant). Coherence and phase results for eastward propagating zonal wavenumber two are generally similar.

These results represent, for midlatitudes, an extension of earlier work of C. R. Mechoso and D. L. Hartmann to phase speeds less than 10 m s^{-1}, for which an interpretation in terms of baroclinic instability becomes viable; a much larger dataset is also used here. The strong coherence found between the subtropics and Tropics lend support to the notion that planetary wave baroclinic instability and the MJO are connected with each other, as suggested by J. S. Frederiksen and C. S. Frederiksen. An origin of the MJO in which subtropical jet instability helps to organize tropical convection is suggested.

1. Introduction

The observational analysis of baroclinic instability has largely concentrated on synoptic-scale phenomena. Nevertheless, there are strong theoretical reasons for expecting significant instabilities at planetary zonal wavenumbers as well. Highly simplified linear stability theory does indeed suggest maximum growth rates for total horizontal wavenumbers of about six, but much of the total wavenumber is due to the meridional scale of the waves, so that this is not incompatible with planetary zonal wave instabilities (Hartmann 1979; Ioannou and Lindzen 1986). Moreover, while studies of baroclinic instability on the sphere with realistic basic states indicate that the shorter waves (zonal wavenumber ~

Corresponding author address: David M. Straus, Center for Ocean–Land–Atmosphere Studies, 4041 Powder Mill Rd., Suite 302, Calverton, MD 20705.
E-mail: straus@cola.iges.org

© 2000 American Meteorological Society

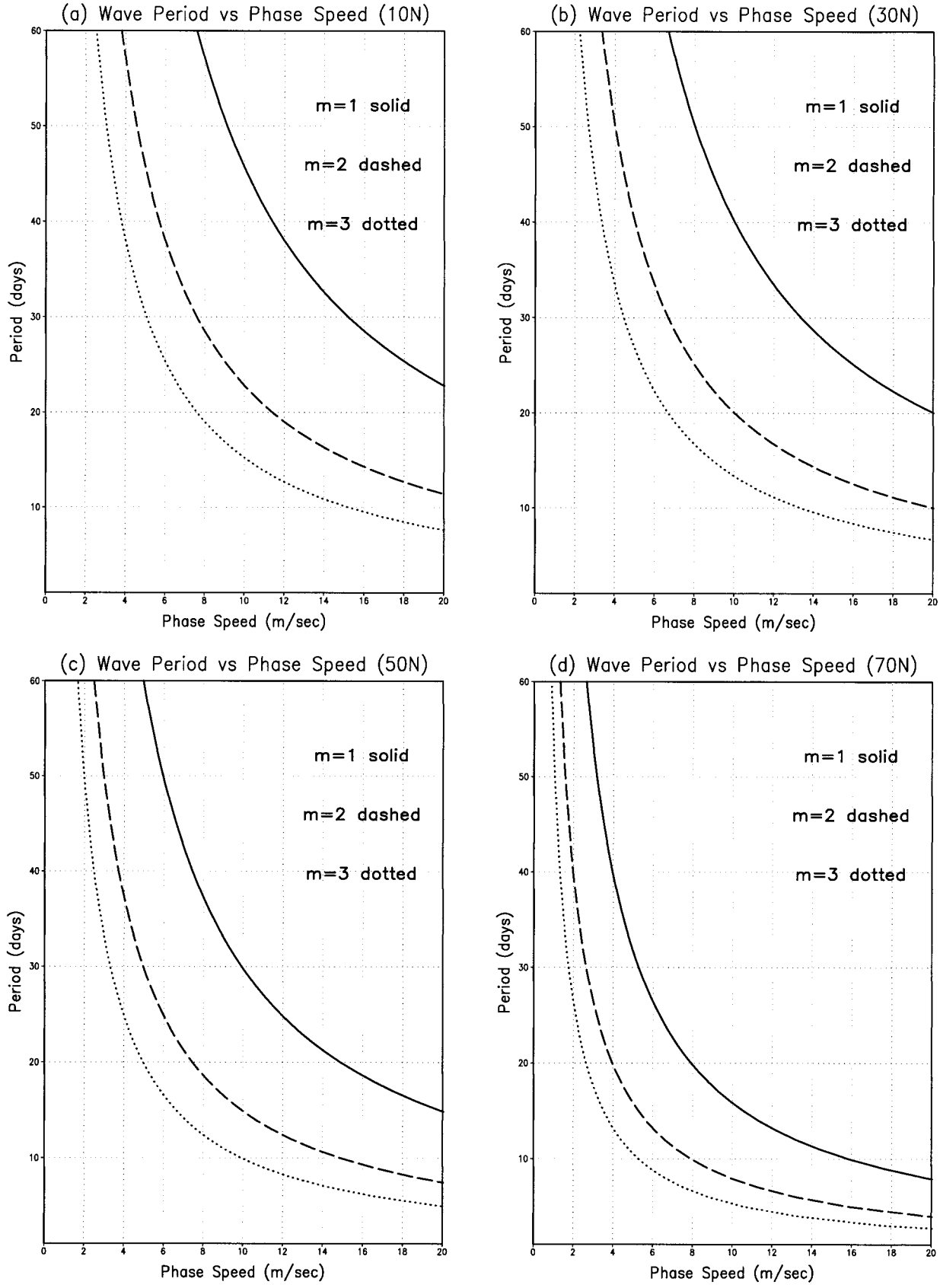
(a) Wave Period vs Phase Speed (10N)
(b) Wave Period vs Phase Speed (30N)
(c) Wave Period vs Phase Speed (50N)
(d) Wave Period vs Phase Speed (70N)
m=1 solid
m=2 dashed
m=3 dotted
Period (days)
Phase Speed (m/sec)
0
2
4
6
8
10
12
14
16
18
20
10
20
30
40
50
60

8–15) are most unstable, it is well known that these waves saturate relatively quickly, and that the more slowly growing longer waves are able to achieve higher amplitudes, particularly in the upper troposphere (Gall 1976a,b; Simmons and Hoskins 1978; see also Straus 1981).

In the presence of β, however, all baroclinically unstable wavenumbers are associated with phase speeds corresponding to eastward propagation and to steering levels near the ground (i.e., 1–10 m s^{-1}) (Pedlosky 1987). The purpose of this paper is to present a uniform and consistent global diagnosis of eastward propagating planetary waves with phase speeds in the range of 1–10 m s^{-1} from atmospheric analyses, and to explore the relationships of these waves with the tropical Madden–Julian oscillation (MJO; Madden and Julian 1971, 1994), which has a very similar range of frequencies. The frequencies of interest imply very long periods and hence require a very long homogeneous dataset in order to be detected with statistical significance. Recent reanalyses such as that from the National Centers for Environmental Prediction (NCEP; Kalnay et al. 1996), in principle, provide such a dataset. Mechoso and Hartmann (1982) have carried out an analysis for the Southern Hemisphere that is similar in spirit to ours; we will discuss the relationship of their work and the current paper in the discussion.

While the natural emphasis of the study of baroclinic instability would be on midlatitudes, eastward propagating waves with phase speeds of 1–10 m s^{-1} have a large overlap with the MJO in the Tropics. In fact, since we present results for the zonal wind (u), the MJO is very prominent in our analysis in tropical regions. Since both potential midlatitude planetary wave instabilities and the MJO will appear on a nearly equal footing in our analysis, both representing low phase speed eastward propagating motions, the issue of tropical–extratropical interactions becomes germane. Knutson and Weickmann (1987) find wavenumber one subtropical features in the streamfunction field associated with the MJO life cycle of outgoing longwave radiation (OLR), and note the relationship of these features to the East Asian jet. Yet such large zonal-scale connections are not found in other observational analyses. Lau and Phillips (1986) studied the relationship between the MJO and midlatitude height and found that it is dominated by wave train–like features with smaller zonal scales, with apparent equatorward propagation from midlatitudes into the tropical western Pacific. The observational results of Liebmann and Hartmann (1984) are in general agreement. They find that 5- and 10-day mean OLR in the central Pacific and 500-hPa height in the Pacific jet region are well correlated at zero lag and when the heights lead the OLR (but not vice versa). Hsu et al. (1990), studying a single winter in which the MJO was particularly active (1985/86) also find evidence of localized extratropical influences on the MJO. These latter authors emphasize that the compositing methodology of Knutson and Weickmann tends to emphasize larger scales. In this paper we focus specifically on planetary wave scales in the zonal direction.

The instability calculation of Frederiksen and Frederiksen (1997, hereafter FF) provides further motivation for our observational work. Utilizing a linear moist two-level model, FF identify (among many modes) an instability that couples the extratropics with a tropical eastward propagating disturbance, baroclinic in nature, which has the frequency of the MJO.

Our approach, including the methodology for distinguishing these slowly traveling waves from vacillations in stationary waves (also known as standing waves) will be described in the following section—as well as in an appendix. Results for eastward propagating planetary scale waves with long periods are presented in sections 3 and 4. A discussion is given in section 5. Perhaps the most interesting relation suggested by this study is that between baroclinic planetary-scale waves in the subtropics and the MJO of the Tropics.

2. Diagnoses of low-frequency baroclinic waves

The approach to defining the datasets and establishing the methods of analysis were guided by the focus on potential longwave baroclinic instabilities, and in particular on waves with well-defined phase speeds consistent with steering levels in the lower troposphere, that is with phase speed c in the range 1–10 m s^{-1}. Consideration of the expression for c,

$$c = \frac{\omega}{k} = \frac{2\pi}{\tau}\frac{a\cos(\phi)}{m}$$

(where ω is angular frequency, k dimensional wavenumber, τ period, φ latitude, a the earth's radius, and m dimensionless zonal wavenumber) reveals that such phase speeds imply very long periods for planetary waves. The wave period τ is plotted against phase speed c for zonal wavenumbers $m = 1$–3 at various latitudes in Fig. 1. For $m = 1$, phase speeds less than 10 m s^{-1} imply periods longer than about 30 days at 50°N. This minimum period ranges from about 16 days at 70°N to 45 days at 10°N. The large periods of interest here completely preclude using monthly mean data to diagnose these baroclinic waves, and further imply severe sampling problems for traditional spectral analysis of seasonal data. In fact the low frequencies implied by $m = 1$ phase speeds in the range of 1–10 m s^{-1} have been

←

FIG. 1. Wave period (in days) plotted against phase speed (in m s^{-1}) following formula in text. The solid curves give wavenumber $m = 1$, the dashed curves $m = 2$ and the dotted curves $m = 3$. (a) Latitude 10°N, (b) latitude 30°N, (c) latitude 50°N, (d) latitude 70°N.

relatively poorly studied in midlatitudes. In the Tropics, there is considerable overlap with frequencies relevant for the MJO, which is considered to have periods of ~30–60 days. For $m = 1$, the lower MJO frequencies are included in the set of low phase speed waves, while for $m = 2$ and $m = 3$ the entire band of MJO frequencies (as well as some higher frequencies) are included.

a. Datasets

In order to achieve reasonable statistical stability for these longwave periods we have utilized data from a fairly large number (39) of long (180-day) boreal winter (austral summer) seasons, obtained from the reanalyses of NCEP (Kalnay et al. 1996). This ensures 78 degrees of freedom per spectral (frequency) component. The boreal winter season was defined to start on 0000 UTC 1 November. Twice daily fields of height, temperature, and zonal and meridional winds at 12 pressure levels were obtained from the National Center for Atmospheric Research on a 2.5° × 2.5° grid for the winters of 1958/58 through 1996/97. The data were interpolated to a Gaussian grid consistent with a triangular spectral resolution retaining 42 waves (T42), and zonal wavenumbers 1–10 extracted using zonal Fourier analysis. The dataset was further reduced by averaging in time over nonoverlapping 5-day periods (pentads).

The annual cycle was calculated by first averaging each of 73 pentads per calendar winter over all 39 winters for each variable. The sum of the time mean and first four Fourier components of this climatological sequence were taken to define the annual cycle, which was subsequently subtracted from each pentad winter dataset.

Fourier analysis in time of the record of 36 pentads for each winter was carried out with a fast Fourier transform, which resolves 18 frequencies with corresponding periods ranging from 180 to 10 days. Although all variables were analyzed, results for the zonal (u) component of the wind are emphasized in this paper.

b. Propagating wave diagnosis

The decomposition of a fluctuating eddy field into a zonal wavenumber/frequency spectrum of eastward and westward propagating components is accomplished by space-time spectral analysis in a unique manner, as we review in the appendix. However, distinguishing physically propagating waves from standing waves is more difficult, since the latter do not appear as components of a space-time Fourier analysis (Pratt 1976; Hayashi 1977). Standing waves refer to temporal fluctuations with geographically fixed nodes, and can be thought of as oscillations of a fixed spatial pattern. At each discrete frequency and zonal wavenumber, a standing wave can be expressed as a sum of an eastward and a westward propagating wave with the same amplitude and phase. In general there is no unique way to separate the standing waves from physically propagating waves. Hayashi (1977) proposed a method of isolating the standing waves that is physically reasonable. In this paper we calculate both the unique variance associated with eastward (westward) propagating components PE (PW), as defined from space-time spectral analysis, and the variance associated with the eastward propagating physical wave PE* defined from Hayashi's method. The term propagating component is used to refer to results from unambiguous space-time spectral analysis, while the term propagating wave is used when the estimated standing wave part has been removed. A full description is given in the appendix.

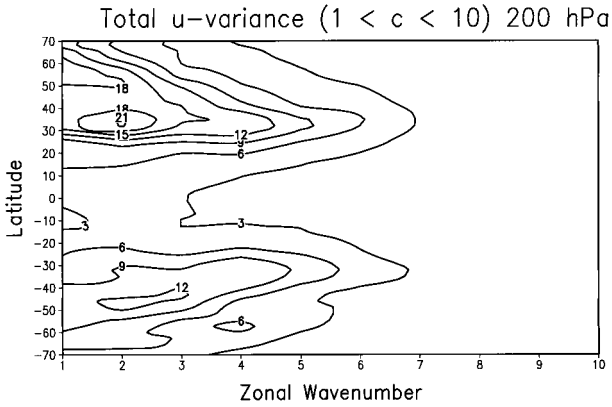

FIG. 2. Total variance in the u wind at 200 hPa summed over frequencies that correspond to phase speeds of 1–10 m s^{-1}, as a function of latitude and zonal wavenumber. Contour interval is 3 m^2 s^{-2}.

3. Eastward propagating variance

Zonal wavenumber spectra of the zonal wind u, presented as a function of latitude for the 200-hPa level in Fig. 2, show the dominance of the longest planetary waves. Here the total variance (PE + PW) is summed over all frequencies corresponding to the range of phase speeds 1–10 m s^{-1}. In the Northern Hemisphere both a peak at wavenumber $m = 2$ at about 32°N (near the subtropical jet), and a peak farther north (at 55°N) at wavenumber one are noted. At 300 hPa (not shown) the subtropical variance is dominated by the strong peak at higher latitudes for $m = 1$ and $m = 2$. This continues to be the case at lower levels (not shown), although the variance diminishes there. In the Southern Hemisphere a less intense maximum appears in midlatitudes for $m = 2$–3 at all levels. Similar plots of the height field (not shown) indicate high latitude maxima for low values of m in place of the midlatitude maxima seen in Fig. 2. The subtropical maximum at 200 hPa is completely missing. Low phase speed planetary fluctuations in midlatitudes and the subtropics are apparently dominated by small meridional scales, and thus are manifest most strongly in the meridional gradient of the height field (geostrophic u wind).

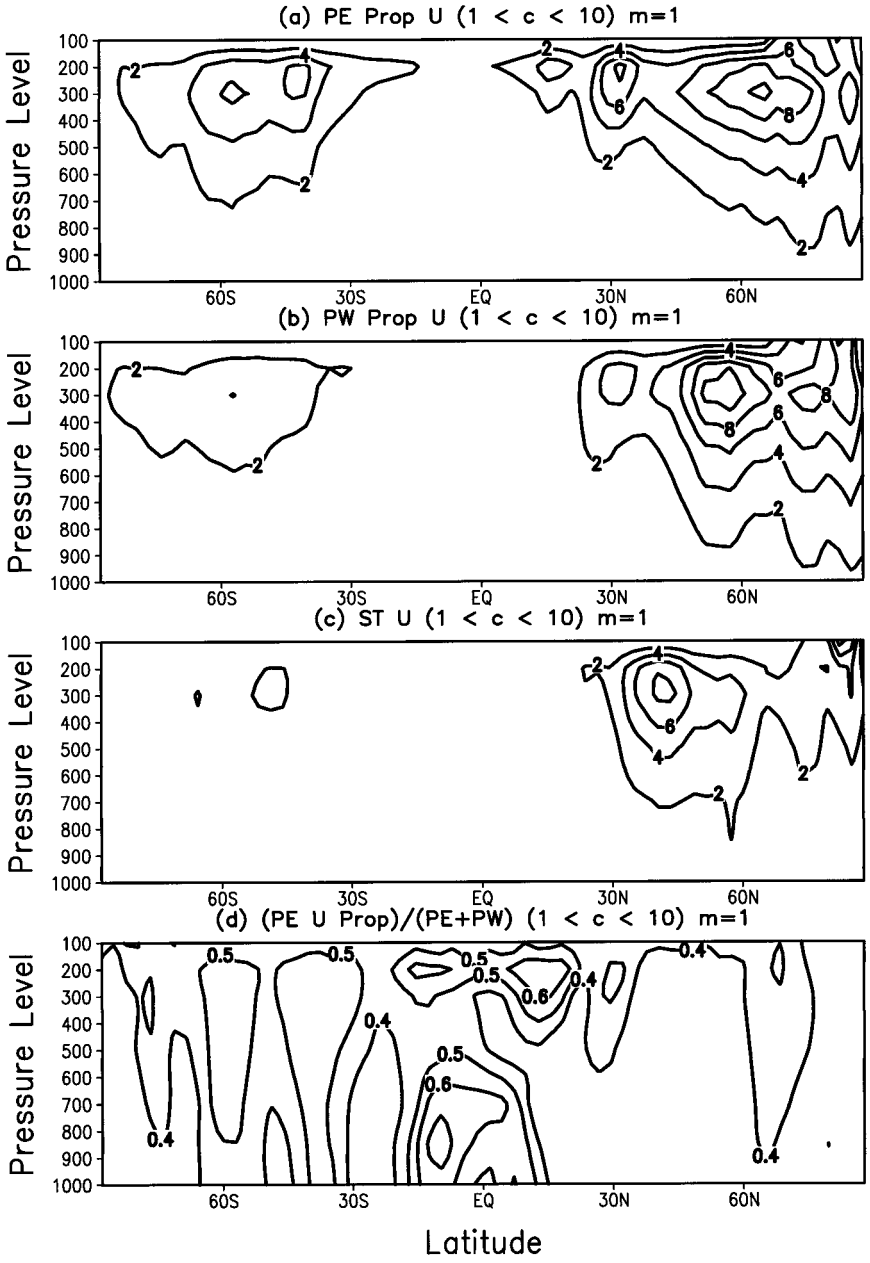

FIG. 3. (a) Eastward propagating wave variance PE* for zonal wavenumber $m = 1$, summed over frequencies that correspond to phase speeds 1–10 m s^{-1}, as a function of latitude and pressure level. (b) Westward propagating wave variance PW*. (c) Standing wave variance ST. (d) Normalized eastward propagating wave variance PE*/(PE + PW).

Spectra of the propagating variances PE and PW for $m = 1$ at upper levels (not shown) indicate that in much of the Southern Hemisphere and in the Tropics, westward propagation is completely dominated by eastward propagation. In fact PW is smaller than the lower limit of the 95% significance band asssociated with PE, where the significance has been calculated using 78 degrees of freedom (Jenkins and Watts 1968). However, in the Northern Hemisphere midlatitudes, where westward propagating low-frequency Rossby planetary waves are active (Madden 1979; Salby 1981a,b; Lindzen et al. 1984; Straus et al. 1987), PE and PW are comparable. In addition, standing oscillations (due to topographic and/or land–sea thermal contrast effects) contribute to both the eastward and westward propagating variance. As described in section 3 and the appendix, the amplitude of the standing oscillations can be estimated and removed. Figure 3 shows the remaining wave variances PE* and PW*, which correspond to eastward and westward propagating waves (respectively), for $m = 1$, as

a function of latitude and pressure level, summed over those frequencies that correspond to phase speeds of 1–10 m s^{-1}. In addition, the variance associated with standing waves ST (summed over the same phase speed range) is given, as well as the normalized wave variance, that is, the ratio of eastward propagating wave variance to total variance, or PE*/(PE + PW). Clear maxima in PE* are seen in the midlatitudes of both hemispheres at 300 hPa, and in the northern subtropics at 200 hPa. In addition, an upper-level tropical maximum is seen in the Tropics north of the equator. Northern Hemisphere 300-hPa maxima in PW* are seen in the subtropics and midlatitudes, although the subtropical peak is weaker than the corresponding PE* peak. The standing wave variance is confined to northern midlatitudes at 200 hPa and high latitudes (100 hPa). The northern subtropical maximum of PE* accounts for 50% of the total variance. In the Tropics, maxima of 60%–70% in the normalized variance are seen both at upper levels (15°N and 15°S) and at lower levels (at about 10°S). These tropical features are consistent with the MJO (Madden and Julian 1971, 1994; Knutson and Weickmann 1987), which dominates the tropical intraseasonal variability. It is interesting that the plot equivalent to Fig. 3d for the height field (not shown), which might not be expected to yield any distinct features in the Tropics, indicates tropical maxima in the normalized variance similar to those in Fig. 3d. The normalized wave variance is thus a sensitive indicator of the dominant tropical planetary wave intraseasonal oscillation.

Figure 4 for $m = 2$ reveals features for PE* that are similar to $m = 1$ in the subtropics and midlatitudes, although features in the southern subtropics are more distinct. In the Tropics a maximum appears at 200 hPa, just south of the equator, where it explains over half the total variance, while the tropical maximum north of the equator seen in Fig. 3a is now missing. The westward propagating wave variance PW* is very similar to its $m = 1$ counterpart (without, however, the subtropical peak), while the standing wave variance ST is weaker. The normalized wave variance for $m = 2$ is similar to that for $m = 1$ in the Southern Hemisphere, but lacks the distinct upper-level peak north of the equator seen in the previous figure.

The meridional structure of the wave variance PE* summed over frequencies corresponding to low phase speeds (as presented above) is compared to that of PE* summed over the MJO frequencies (periods of 30–60 days) for $m = 1$ at 200 and 300 hPa in Figs. 5a and 5b. The similarity of these variances in the Tropics and subtropics indicates the dominance of phase speeds between 6 and 10 m s^{-1} (see Fig. 1). The normalized eastward propagating wave variance for the MJO frequency band (Fig. 5c) is very similar in structure to the same quantity shown for low phase speeds in Fig. 3d, with slightly higher magnitudes in the Tropics. In midlatitudes, however, the relatively low MJO variance indicates that very low phase speeds (with periods exceeding 60 days) dominate. Explicit calculation of the phase speed spectra (not shown) confirms these observations.

Figure 6 compares the low phase speed PE* with the MJO PE* for $m = 2$, with results generally similar to those in Fig. 5. However, even in the subtropics the MJO variance is only about 50% of the total low phase speed variance.

4. Coherence and phase structure

In order to assess the interdependence of eastward propagating fluctuations at various locations, we examine the coherence (squared) of the eastward propagating components in the *u* wind between a base latitude and level and all other latitudes and levels. As discussed in the appendix, this calculation is based on the cross spectrum of eastward propagating components without any correction for standing waves. In addition, since an oscillation of a single frequency corresponds to two distinct phase speeds at two latitudes, it is not possible to infer a true phase-speed cross spectrum from the usual frequency cross spectrum of time series at different latitudes. The results presented here are based on cross spectra between pairs of points (in the latitude/pressure plane) averaged over those frequencies that represent phase speeds in the range 1–10 m s^{-1} for *both* latitudes. We refer to this as restricted frequency averaging. The results are compared to those based on cross spectra averaged uniformly over all MJO frequencies (periods of 30–60 days). The coherence squared and phase were calculated using the averaged complex cross spectrum in the both cases, as described in the appendix.

The squared coherence and phase between eastward propagating fluctuations for $m = 1$ at a base point to 52°N and 300 hPa and all other locations are given in Fig. 7a, using restricted frequency averaging. The squared coherence is plotted with a contour interval of 0.1, with a minimum of 0.3.[1] The arrows indicate the phase angle, plotted so that a rightward pointing arrow corresponds to 0°, meaning no phase shift, while an arrow pointing in the first quadrant corresponds to a positive phase shift, that is the ridge of the wave at the indicated latitude/level lies to the east of that at the base latitude/level. Similarly a 90° shift (series leads the base point by 90°) corresponds to an upward-pointing arrow, and a 180° shift (series out of phase with base point) corresponds to a leftward-pointing arrow. The length of the arrows is proportional to the squared coherence. The

[1] Note that since there are 78 degrees of freedom for each frequency component (2 degrees of freedom for each year), we conservatively estimate that the null hypothesis of no coherence can be rejected at the 99% significance level for coherence squared values greater than 0.11 according to Julian (1975). Since a number of frequencies are averaged together, the number of degrees of freedom actually exceeds 78.

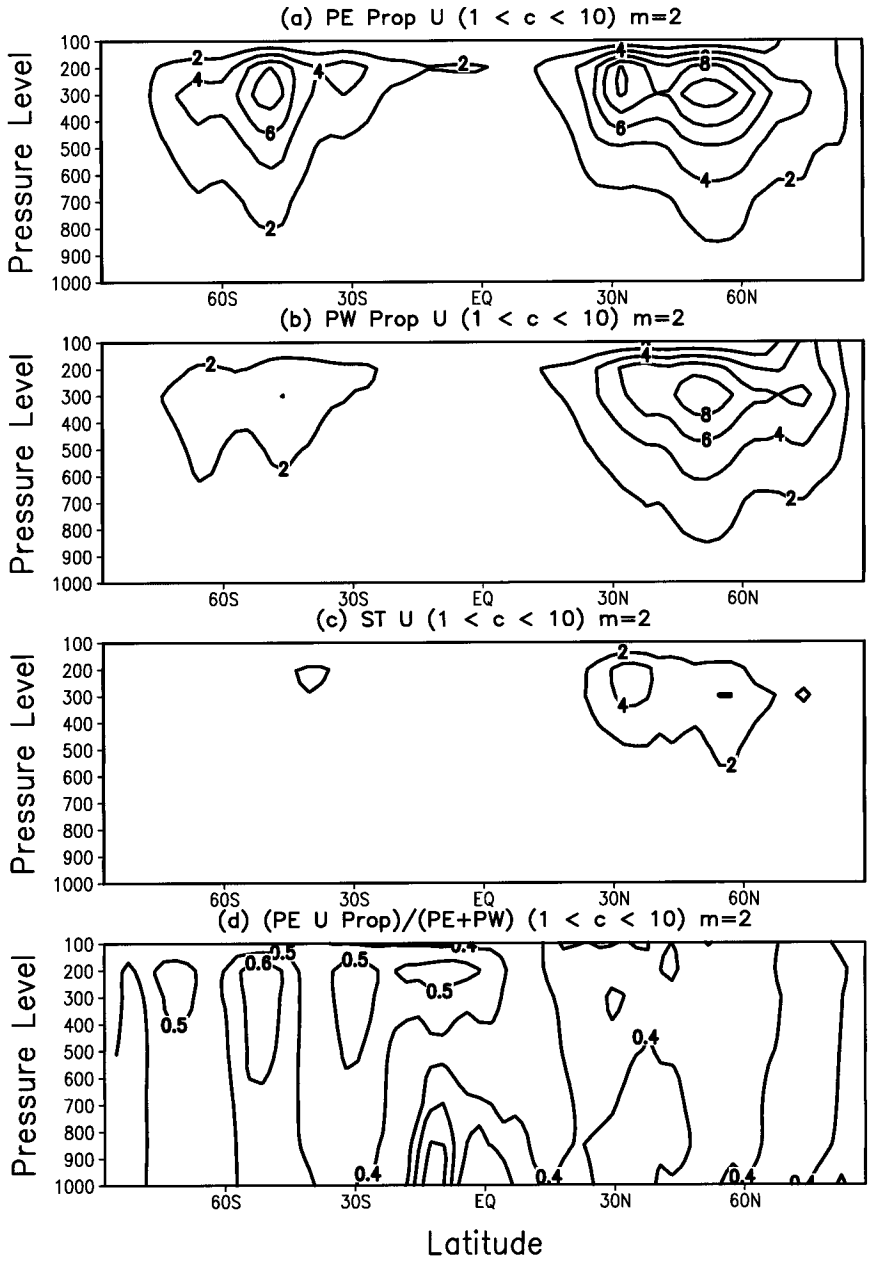

FIG. 4. As in Fig. 3 but for zonal wavenumber $m = 2$.

results for the MJO frequency averaging (not shown) are nearly identical. Besides the (expected) large coherence near the base point at 52°N, there is a region of strong coherence (squared coherence exceeding 0.60) near 30°N, which tilts slightly poleward with increasing height. The arrows indicate that this subtropical region is almost exactly out of phase with the base point, while the sense of the arrows in the lower troposphere at 52°N indicate a slight westward phase tilt with height there.

Figure 7b shows the $m = 1$ coherence and phase with respect to a base point at 32°N and 200 hPa, corresponding to the peak in eastward propagating wave variance seen in Fig. 3. Again results for the restricted frequency averaging shown in the figure and the MJO averaging (not shown) are almost identical. Fluctuations at this subtropical base point are strongly coherent with upper-level tropical fluctuations at 13°N (squared coherence > 0.70), where maxima in both PE* and normalized variance are indicated in Fig. 3. The subtropical and tropical fluctuations are almost completely out of phase. Consistent with Fig. 7a, there is also a maximum in coherence squared with points at 52°N with an out of phase relationship.

That the strong maximum in relative eastward wave

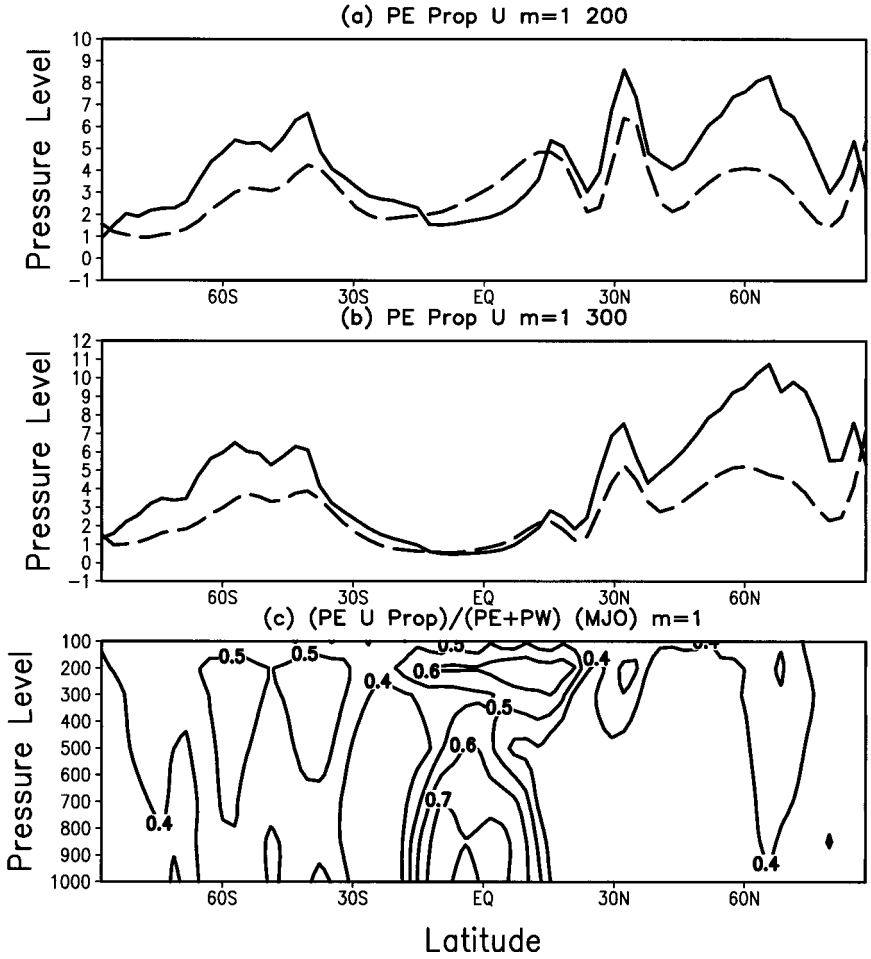

FIG. 5. (a) Eastward propagating wave variance PE* at 200 hPa for zonal wavenumber $m = 1$, summed over frequencies that correspond to phase speeds 1–10 m s^{-1} (solid line), and summed over MJO frequencies (corresponding to periods of 30–60 days, dashed line). (b) Same as in (a) but for 300 hPa. (c) Normalized eastward propagating wave variance, PE*/(PE + PW), where each term is summed over MJO frequencies.

variance at 13°N is related to the MJO is suggested by Figs. 8 and 9, which give the coherence and phase with respect to the tropical base point at 13°N and 13°S at 200 hPa, with both MJO and restricted frequency averaging now shown. In each case a strong squared coherence is seen with fluctuations at lower levels just south of the equator, with a nearly out of phase relationship between upper and lower levels. This decidedly baroclinic vertical structure is in stark contrast to the nearly barotropic structure seen in the subtropics and midlatitudes. For the base point at 13°N (Figs. 8a and 8b), the maximum coherence is seen at 700 hPa and is stronger for the MJO averaging than for the restricted averaging, although the latter coherence squared exceeds 0.50. For the base point at 13°S, the maximum coherence is at a lower level. The MJO frequency averaging in Figs. 8a and 9a also shows significant coherence across the equator at upper levels with an in-phase relationship. The tropical phase relationships shown here are consistent with the distinct signature of the MJO (Knutson and Weickmann 1987). That the cross-equatorial upper-level coherence is not seen in the restricted frequency averages (Figs. 8b and 9b) indicates that there is variance for phase speeds less than about 7 m s^{-1}, but that this very low-frequency signal (periods greater than 60 days) does not have cross-equatorial coherence.

The results for the base point at 200 hPa in the Southern Hemisphere subtropics (at 32°S, Fig. 10a) are in general similar to those at 32°N (Fig. 7b) but the coherence with the Tropics is significantly weaker, with squared coherence reaching only 0.30. Note also that PE* is weaker in the southern Tropics and subtropics than it is north of the equator (Fig. 3). On the other hand, the Southern Hemisphere midlatitude 300-hPa coherence and phase relationships (base point of 52°S, Fig. 10b) are almost a mirror image of the results for the Northern Hemisphere of Fig. 7a. The MJO frequency

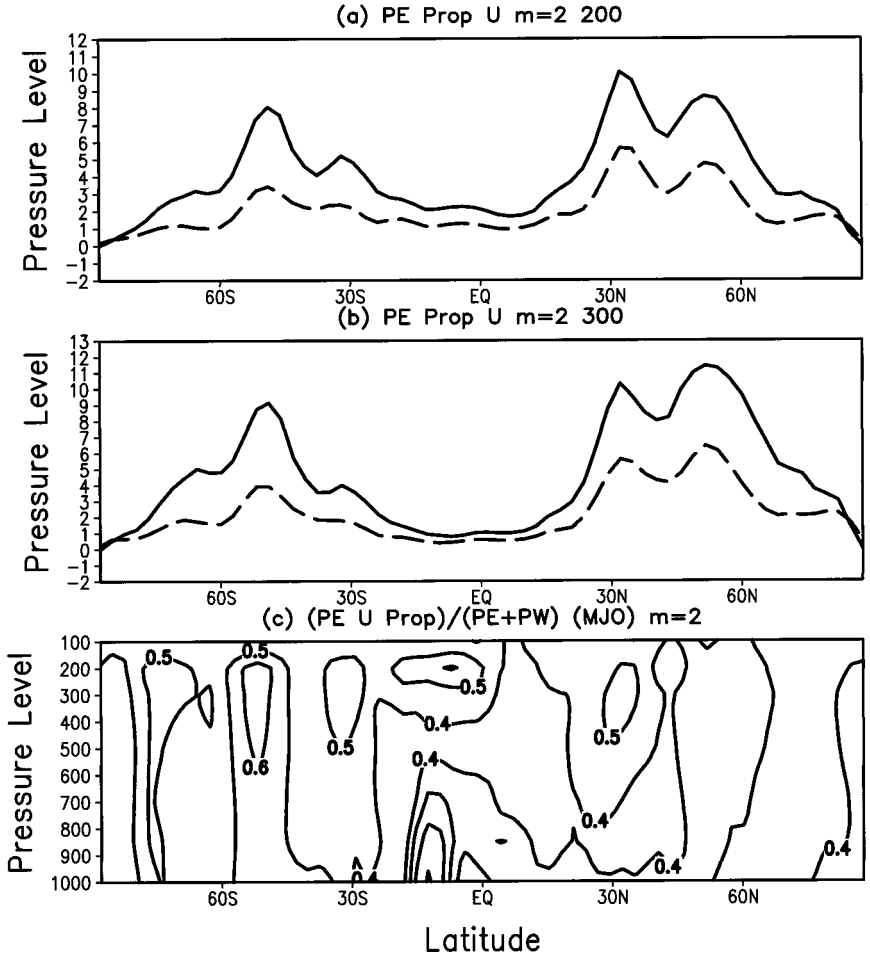

FIG. 6. As in Fig. 5 but for zonal wavenumber $m = 2$.

averaging and the restricted frequency averaging give nearly identical results for base points at 32°S and 52°S. Only the latter are shown in Fig. 10.

Coherence and phase results for zonal wavenumbers $m = 2$ are summarized in Fig. 11, which shows results with respect to base points at 32°N, 13°N, 13°S, and 32°S at 200 hPa. Figures 11a–d show the results of the restricted frequency averaging, which are nearly identical to the results obtained averaging over the MJO frequencies, shown in Figs. 11e–h. The strong relationship between midlatitude and subtropical eastward propagating fluctuations seen in $m = 1$ holds equally well for $m = 2$. The $m = 1$ strong coherence and out-of-phase relationship between northern subtropical and tropical off-equatorial eastward propagating fluctuations is substantially maintained for $m = 2$ (Figs. 11b and 11f). But the strong tropical coupling of the upper levels just north of the equator to lower levels (and the coherence across the equator for the MJO averaging) is not seen for $m = 2$. Once we move into the Southern Hemisphere, the strong MJO coupling between upper and lower levels south of the equator is preserved (cf. Figs. 11c and 11g with Fig. 9).

Note that because of the lesser variance PE* for $m = 2$ (and $m = 3$, not shown) in the subtropics and particularly the Tropics compared to $m = 1$, the magnitude of the complex cospectrum, giving the actual covariance of eastward propagating series within the frequency band of interest, does decrease fairly strongly with increasing m (not shown).

5. Discussion

The coherence structures seen with respect to midlatitude base points for the planetary waves are similar to those shown by Mechoso and Hartmann (1982, hereafter MH), who examine eastward propagating waves in the Southern Hemisphere during one southern winter, while we have examined 39 boreal winters (southern summers). The coherence between midlatitudes and subtropics shown by MH is not as strong as seen in Fig. 10a and for $m = 1$ the meridional scale is

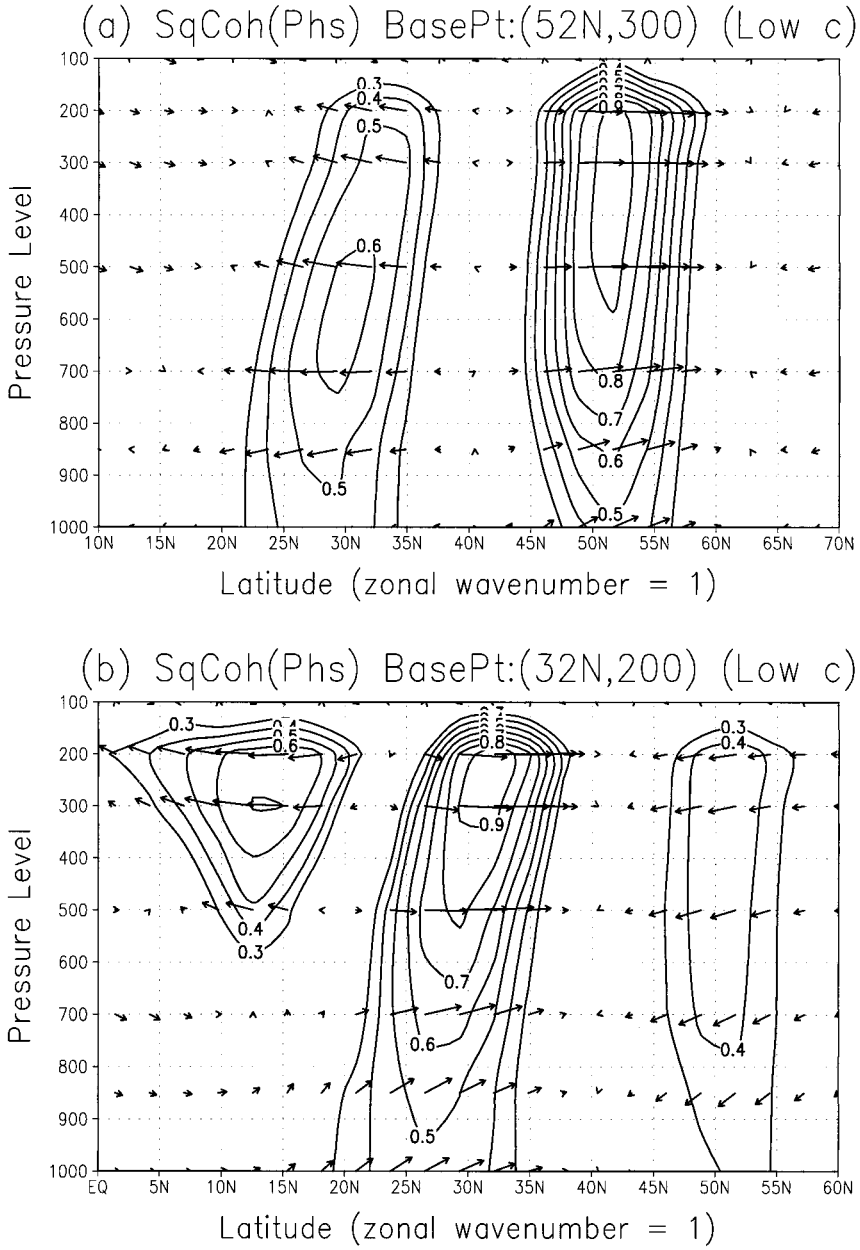

FIG. 7. (a) Squared coherence (contours) and phase (arrows) of eastward propagating fluctuations for zonal wavenumber $m = 1$ with respect to a base point of 52°N and 300 hPa, as a function of latitude and pressure level. The squared coherence and phase are calculated from co- and quadrature spectra that have been averaged over frequencies corresponding to phase speeds of 1–10 m s^{-1}. See the appendix. Arrows pointing to the right indicate no phase shift, arrows pointing in the first quadrant mean that the indicated point leads the base point (wave ridge to the east of the base point), etc. The length of the arrows is proportional to the squared coherence. (b) As in (a) but for eastward propagating zonal wavenumber $m = 1$ fluctuations with respect to a base point of 32°N and 200 hPa.

broader than is indicated in our results. While MH interpret the structure they find in terms of a baroclinically unstable mode of the ''Charney–Eady'' type, the wave periods involved (15 days for $m = 1$, 7.5 days for $m = 2$) imply phase speeds greater than 10 m s^{-1} and thus steering levels in the upper troposphere, although the zonally averaged u wind tends to be stronger in southern winter than in northern winter. It is interesting that by explicitly restricting phase speeds to be less than 10 m s^{-1}, feasible only because of the very large dataset used here, we find the same overall structure but with stronger midlatitude/subtropical coher-

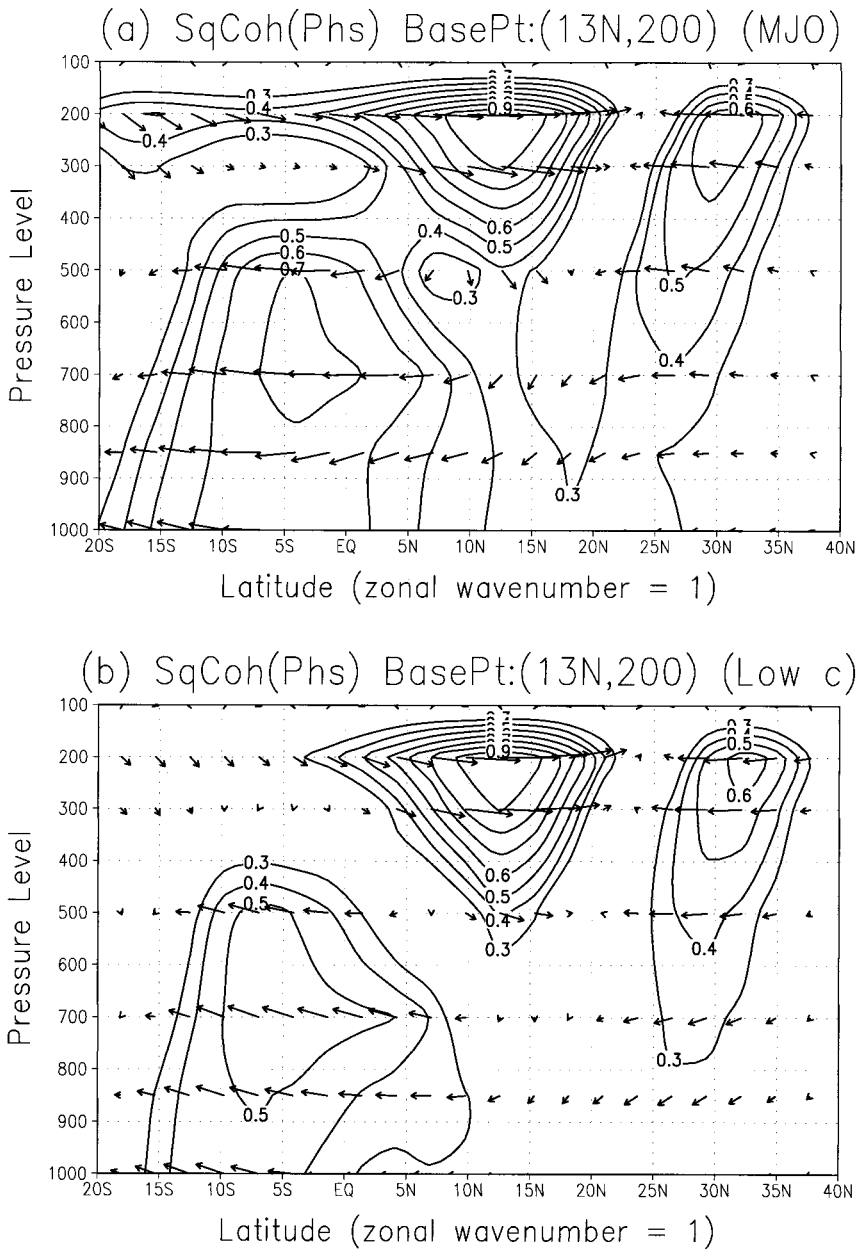

FIG. 8. (a) Squared coherence (contours) and phase (arrows) of eastward propagating fluctuations for zonal wavenumber $m = 1$ with respect to a base point of 13°N and 200 hPa, as a function of latitude and pressure level. The squared coherence and phase are calculated from co- and quadrature spectra that have been averaged over the MJO frequencies corresponding to periods of 30–60 days. See the appendix. Arrows pointing to the right indicate no phase shift, arrows pointing in the first quadrant mean that the indicated point leads the base point (wave ridge to the east of the base point), etc. The length of the arrows is proportional to the squared coherence. (b) As in (a) but with squared coherence and phase calculated from averages over frequencies corresponding to phase speeds of 1–10 m s^{-1}.

ence. While this is consistent with an important role played by baroclinic instability, it is in general problematic to interpret observed results with purely linear theory; in general we expect to observe only the equilibrated nonlinear waves.

What has been brought into focus in our results is the finding of strong coherence between eastward propagating waves in the *u* wind in the subtropics and the Tropics at upper levels, as seen especially in those plots with base points in the subtropics and Tropics (Figs. 7b, 8, 9, 10a, and 11). The strong similarity between the tropical and subtropical phase relationships between the

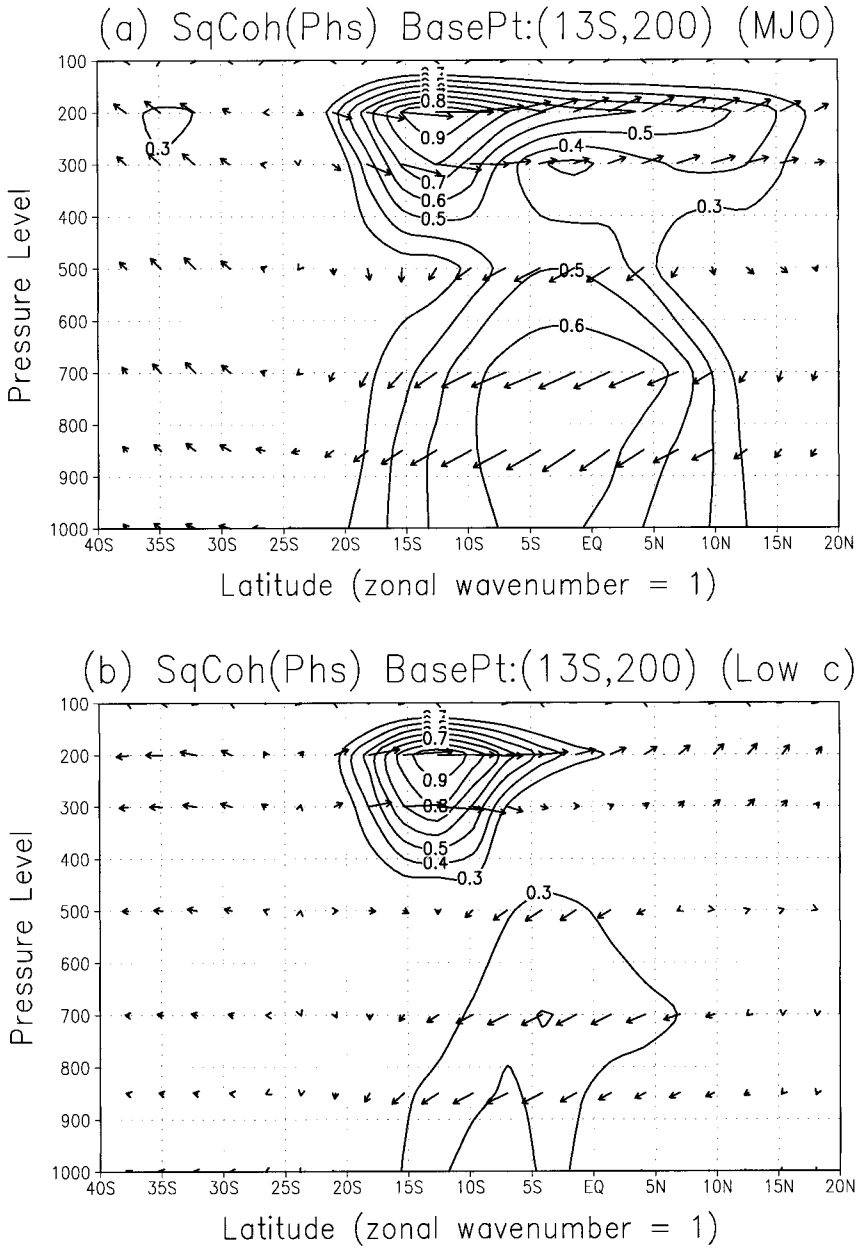

FIG. 9. (a) Squared coherence (contours) and phase (arrows) of eastward propagating fluctuations for zonal wavenumber $m = 1$ with respect to a base point of 13°S and 200 hPa, as a function of latitude and pressure level. The squared coherence and phase are calculated from co- and quadrature spectra that have been averaged over the MJO frequencies corresponding to periods of 30–60 days. See the appendix. Arrows pointing to the right indicte no phase shift, arrows pointing in the first quadrant mean that the indicated point leads the base point (wave ridge to the east of the base point), etc. The length of the arrows is proportional to the squared coherence. (b) As in (a) but with squared coherence and phase calculated from averages over frequencies corresponding to phase speeds of 1–10 m s^{-1}.

low phase speed and MJO frequency averaging raises the possibility that the MJO and planetary-scale instabilities may be linked; the frequencies participating in the important phase relationships are common to both. These results put on a firmer footing the findings of Knutson and Weickmann (1987) regarding the planetary zonal scale of extratropical–MJO interactions. Other recent diagnostic studies relating midlatitude fluctuations with the MJO (Schubert and Park 1991; Hsu 1996) emphasize the structure and evolution of the midlatitude patterns that are statistically related to the tropical convection on the 30–60-day timescale. These essentially

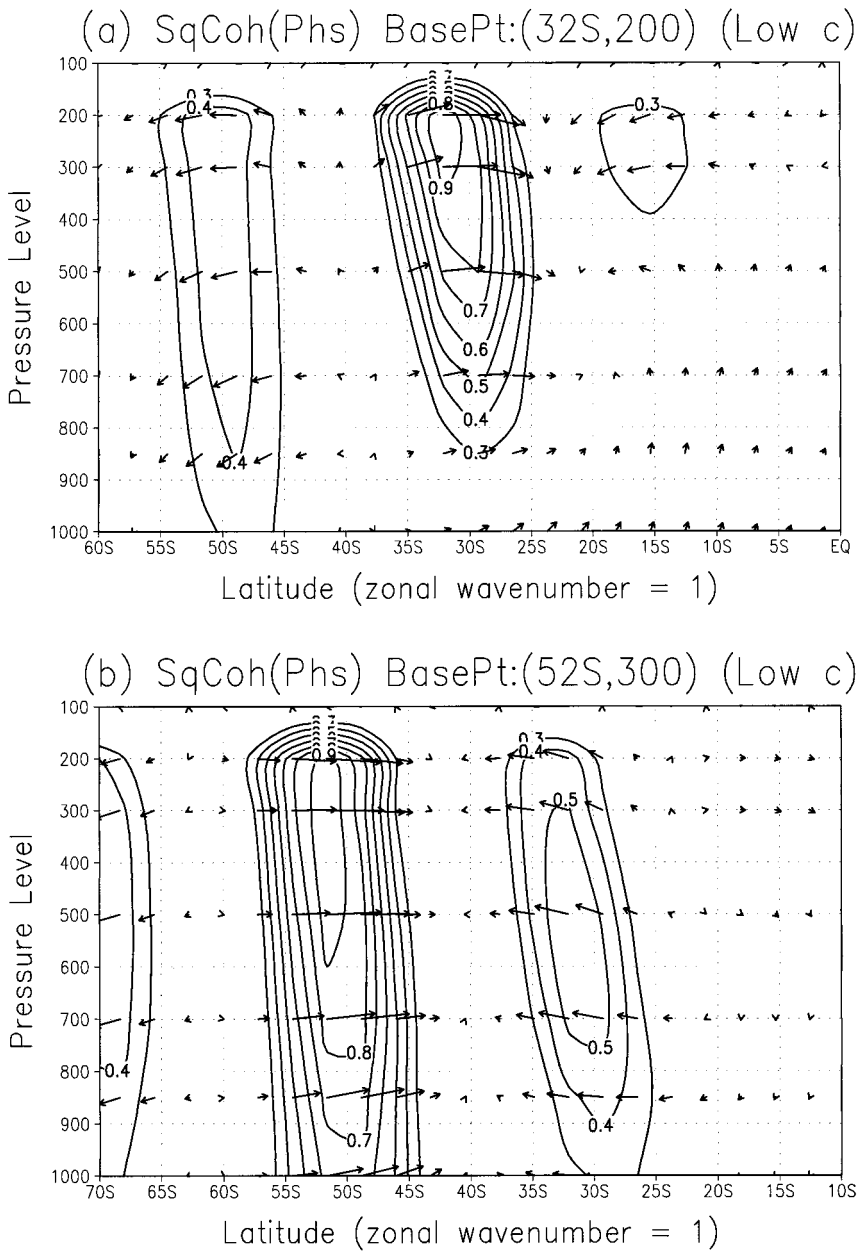

FIG. 10. (a) Squared coherence (contours) and phase (arrows) of eastward propagating fluctuations for zonal wavenumber $m = 1$ with respect to a base point of 32°S and 200 hPa, as a function of latitude and pressure level. The squared coherence and phase are calculated from co- and quadrature spectra that have been averaged over frequencies corresponding to phase speeds of 1–10 m s^{-1}. See the appendix. Arrows pointing to the right indicate no phase shift, arrows pointing in the first quadrant mean that the indicated point leads the base point (wave ridge to the east of the base point), etc. The length of the arrows is proportional to the squared coherence. (b) As in (a) but for eastward propagating zonal wavenumber $m = 1$ fluctuations with respect to a base point of 52°S and 300 hPa.

linear analyses tend to emphasize local, standing oscillations and wave trains, in contrast to the present work.

Our results suggest that planetary-scale baroclinic instability may be linked to the MJO, although, as with previous observational studies, the direction of influence cannot be inferred from the present analysis. The strong coherence between fluctuations near the subtropical jet in the Northern Hemisphere, as well as the fact that the *u* wind seems to carry the signal, suggest that combined baroclinic instability of the jet is involved with modifications (primarily meridional concentration and confinement) due to the barotropic shear in the jet (Ioannou

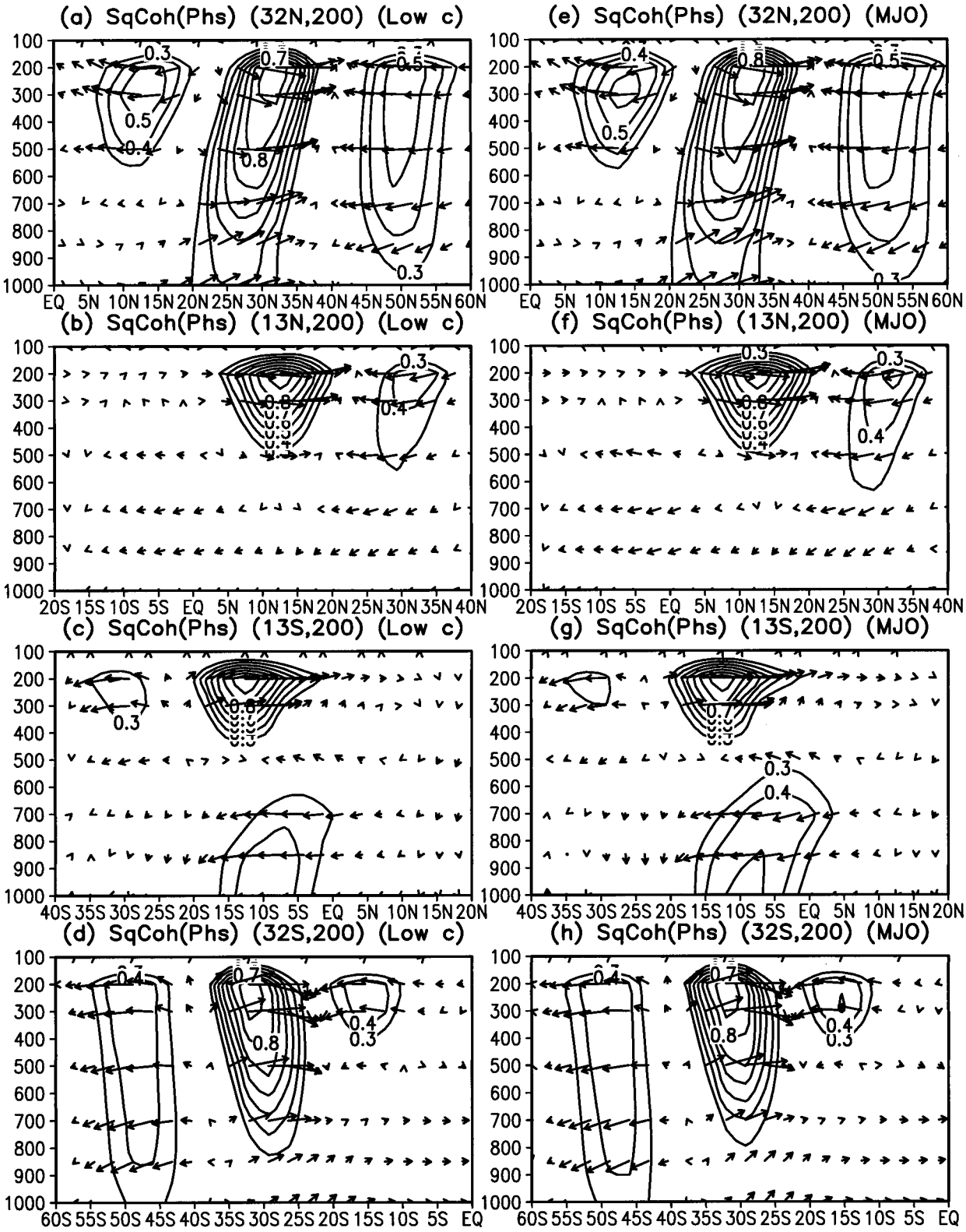

FIG. 11. (a) Squared coherence (contours) and phase (arrows) of eastward propagating fluctuations for zonal wavenumber $m = 2$ with respect to a base point of 32°N and 200 hPa, as a function of latitude and pressure level. The squared coherence and phase are calculated from co- and quadrature spectra that have been averaged over frequencies corresponding to phase speeds of 1–10 m s^{-1}. Arrows pointing to the right indicate no phase shift, arrows pointing in the first quadrant mean that the indicated point leads the base point (wave ridge to

and Lindzen 1986). Presumably, the baroclinically unstable disturbance acts to modulate convection in the Tropics where convection is concentrated for independent reasons (namely, the presence of moist convective instability) despite the fact that the baroclinic instability itself maximizes at higher latitudes. That baroclinic instabilities can penetrate into the Tropics where they can contribute to the organization of convection has been demonstrated by FF in the context of a two-layer model. The extension to a continuous system remains to be explored. The process hypothesized will produce a wave in convection resulting in latent heating, which will force a secondary component of the wave. The resulting disturbance will, of course, no longer have the appearance of a simple baroclinically unstable mode. The present hypothesized theory for the MJO is consistent with the recent modeling results of Lin et al. (2000), wherein suppression of extratropical baroclinic instability also acted to suppress the MJO, although their results relate to the manifestation of the MJO directly on the equator, while our results emphasize the off-equatorial manifestations. This difference in emphasis may be a consequence of the highly simplified two-level vertical structure assumed in the model of Lin et al.

The present hypothesized theory for the MJO is similar to that proposed by FF, and differs completely from earlier attempts at explanation using CISK (Lindzen 1974; Stevens and Lindzen 1978; Chang and Lim 1988). In fact FF ensured that the relevant moist static stability parameter was positive everywhere, so that within the two-level model context pure wave-CISK instability was not possible. The situation we envision also follows Miller and Lindzen (1992) in viewing an independent and dry[2] flow instability organizing rainfall that would occur anyway into a wave pattern. Both approaches have the advantage of seeking the origin of the MJO frequency in the well-established properties of baroclinic instability.

Acknowledgments. We wish to acknowledge discussions with Duane Waliser, and thank David Neelin for showing us the preprint of Lin et al. (2000). We also wish to acknowledge the helpful suggestions of the late Y. Hayashi. His valuable advice will be missed. Finally, we wish to thank an anonymous reviewer for informing us of the Frederiksen and Frederiksen reference. The work of D. Straus has been supported by Grants ATM 93-21354 from the National Science Foundation (NSF), NA 76 GP 0258 from the National Oceanic and Atmospheric Administration, and NAG 5-4977 from the National Aeronautics and Space Administration (NASA). The work of R. S. Lindzen has been supported by Grants ATM 9421195 from NSF, DE-FG02-93ER61673 from DOE, and NAG5-6304 from NASA.

[2] In the terms of FF, this means a flow instability that needs only the dry static stability for its definition.

APPENDIX

Spectral Analysis of Transients

The general description of the transient eddy field in terms of a complete set of eastward and westward propagating components, and space–time cross spectral analysis based on these components, are described in section a. The relationships between the space–time spectral analysis and one-dimensional Fourier analysis are given in section b. Standing oscillations, that is fluctuations with fixed spatial nodes, are composed of a sum of the fundamental eastward and westward propagating components with equal amplitudes and phases. There is no unique way of distinguishing these standing oscillations from true propagating waves (Pratt 1976; Hayashi 1977). The theory of Hayashi (1977), reviewed in section c, accomplishes this separation but requires assumptions. We use the term ''wave'' to refer to propagating components once the estimate of the standing oscillations has been removed.

a. Space–time cross-spectral analysis

The analysis starts by writing the transient eddy portion of a field $u(\lambda, t)$ as a function of longitude λ and time t in terms of zonal wavenumbers m and discrete frequencies ω_n as

$$u(\lambda, t) = \sum_{m>0} \sum_{n>0} [u^E(\lambda, t) + u^W(\lambda, t)], \quad \text{(A1)}$$

with

$$u^W(\lambda, t) = a^W(m, n) \cos[\omega_n t + m\lambda + \phi^W(m, n)]$$

$$u^E(\lambda, t) = a^E(m, n) \cos[\omega_n t - m\lambda + \phi^E(m, n)]. \quad \text{(A2)}$$

Here ω_n is related to the index n by

$$\omega_n = 2\pi n/T \quad \text{(A3)}$$

and T is the record length (in this case 180 days). In Eqs. (A1) and (A3), $a^W(m, n)$ and $a^E(m, n)$ are the amplitudes of the westward and eastward propagating components, respectively, for frequency ω_n and zonal wavenumber m. Similarly, $\phi^W(m, n)$ and $\phi^E(m, n)$ define the component phases. For eastward propagation, ϕ^E/m gives the longitude of the ridge at $t = 0$. It is important

←

FIG. 11. (*Continued*) the east of the base point), etc. The length of the arrows is proportional to the squared coherence. (b) As in (a) but for base point at 13°N. (c) As in (a) but for base point at 13°S. (d) As in (a) but for base point at 32°S. (e)–(h) As in (a)–(d) but the frequency averaging has been done over MJO frequencies.

to note that the sums in Eq. (A1) include only positive values of the integer indices m and n. [As in Straus and Shukla (1981) the largest allowed values of n and m should be treated slightly differently, but they play no role in the analysis of this paper.] It is useful to write Eq. (A1) in a slightly different form:

$$u(\lambda, t) = \mathrm{Re}[U^W(m, n) + U^E(m, n)], \quad \text{(A4)}$$

where the complex quantities U^W and U^E are

$$U^W(m, n) = a^W(m, n) \exp\{i[\omega_n t + m\lambda + \phi^W(m, n)]\}$$
$$U^E(m, n) = a^E(m, n) \exp\{i[\omega_n t - m\lambda + \phi^E(m, n)]\}. \quad \text{(A5)}$$

The space–time power spectrum is then

$$P(m, n) = \frac{1}{2}U^W(m, n)U^W(m, n)^* + \frac{1}{2}U^E(m, n)U^E(m, n)^*$$
$$= \mathrm{PW}(m, n) + \mathrm{PE}(m, n), \quad \text{(A6)}$$

where an asterisk denotes complex conjugation. From Eq. (A5) we obtain simply

$$\mathrm{PW}(m, n) = \frac{1}{2}[a^W(m, n)]^2$$
$$\mathrm{PE}(m, n) = \frac{1}{2}[a^E(m, n)]^2, \quad \text{(A7)}$$

where PE and PW give the contribution of eastward and westward propagating components to the total time and zonal mean of the square of the original field u, respectively.

Consider now two fields, at different points in the latitude/height plane, which are labeled by the indices r and s. The space–time complex cospectrum between the eastward propagating fields $u_r(\lambda, t)$ and $u_s(\lambda, t)$ is defined as

$$\mathcal{C}^E_{r,s}(m, n) = \frac{1}{2}a^E_r(m, n)a^E_s(m, n) \times \exp\{i[\phi^E_r(m, n) - \phi^E_s(m, n)]\}$$
$$= K^E_{r,s}(m, n) - iQ^E_{r,s}(m, n), \quad \text{(A8)}$$

where K is eastward propagating cospectrum and Q the eastward propagating quadrature spectrum. A similar definition can be given for westward propagating fields; the general space–time complex cospectrum is just the sum of eastward and westward progagating parts.

To motivate these definitions of the space-time cospectrum and quadrature spectrum, we temporarily restrict consideration to eastward propagation at only one frequency and wavenumber and write the two series $u_r(\lambda, t)$ and $u_s(\lambda, t)$ as

$$u_r = a_r \cos(\omega_n t - m\lambda + \phi + \delta)$$
$$u_s = a_s \cos(\omega_n t - m\lambda + \phi), \quad \text{(A9)}$$

thus giving δ as the phase of the first series with respect to the second. From Eq. (A8) we then have

$$K_{r,s} = +a_r a_s \frac{1}{2}\cos(\delta) \qquad Q_{r,s} = -a_r a_s \frac{1}{2}\sin(\delta). \quad \text{(A10)}$$

It is easy to show that the zonal- and time-cross correlation for longitude lag Λ and time lag τ given by

$$R_{r,s}(\Lambda, \tau) = \frac{1}{2\pi}\int_0^{2\pi} d\lambda \frac{1}{T}\int_0^T dt[u_r(\lambda + \Lambda, t + \tau)u_s(\lambda, t)] \quad \text{(A11)}$$

becomes simply

$$R_{r,s}(\Lambda) = K_{r,s}\cos(\omega_n\tau - m\Lambda) + Q_{r,s}\sin(\omega_n\tau - m\Lambda) \quad \text{(A12)}$$
$$= \mathrm{Re}[(K_{r,s} - iQ_{r,s})e^{i(\omega_n\tau - m\Lambda)}]$$
$$= \mathrm{Re}[\mathcal{C}^E_{r,s}(m, n)e^{i(\omega_n\tau - m\Lambda)}]. \quad \text{(A13)}$$

It is not hard to see that if many frequency components n and zonal wavenumbers m are kept, the right-hand side of Eq. (A13) becomes a sum over all n and m, thus emphasizing the Fourier transform nature of the relationship between the cross-correlation function and the complex cospectrum. Note that if *both* eastward and westward propagating fluctuations are retained, the cross-correlation $R_{r,s}$ contains, in addition to the sum of the transforms of $\mathcal{C}^E_{r,s}(m, n)$ and $\mathcal{C}^W_{r,s}(m, n)$, interference terms between them. (These interference terms vanish only for zero space and time lag.) This is related to the presence of standing waves, which are discussed in section c.

As with all spectral quantities, the sampling error can be reduced by averaging $K^E_{r,s}(m, n)$ and $Q^E_{r,s}(m, n)$ over independent samples and adjacent frequencies. Here such averaging is denoted by an overbar. For such averaged quantities, we define the space–time coherence CH and phase PH (for eastward propagation) as

$$[\mathrm{CH}^E_{r,s}(m, n)]^2 = ([\overline{K^E_{r,s}(m, n)}]^2 + [\overline{Q^E_{r,s}(m, n)}]^2) \times ([\overline{\mathrm{PE}_r(m, n)}]^2[\overline{\mathrm{PE}_s(m, n)}]^2)^{-1/2} \quad \text{(A14)}$$

and

$$\tan[\mathrm{PH}^E_{r,s}(m, n)] = -\overline{Q^E_{r,s}(m, n)}/\overline{K^E_{r,s}(m, n)}. \quad \text{(A15)}$$

b. Relationship to one-dimensional analysis

Both in terms of practical calculation, and as a basis for the theory of standing waves of Hayashi (1977), it useful to relate the quantities introduced in section a to one-dimensional transforms. To start, we write the transient eddy field $u(\lambda, t)$ as

$$u(\lambda, t) = \sum_{m>0}[c_m(t)\cos(m\lambda) + s_m(t)\sin(m\lambda)], \quad \text{(A16)}$$

where again m is zonal wavenumber, and the real co-

efficients c_m and s_m depend on time. (It is easy to obtain these coefficients for each discete time directly from a fast Fourier transform.) The one-dimensional Fourier transforms of the ordinary time series $c_m(t)$ and $s_m(t)$ for each fixed m are written as

$$c_m(t) = \sum_{n>0} [C^A_{m,n} \cos(\omega_n t) + C^B_{m,n} \sin(\omega_n t)]$$
$$s_m(t) = \sum_{n>0} [S^A_{m,n} \cos(\omega_n t) + S^B_{m,n} \sin(\omega_n t)], \quad \text{(A17)}$$

where again the coefficients $C^A_{m,n}$ and so forth are real. The connection with the representation given in Eq. (A2) is [as in Straus and Shukla (1981) but with slightly different notation]

$$[a^W(m, n)]^2 = \frac{1}{4}[(C^A_{m,n} - S^B_{m,n})^2 + (S^A_{m,n} + C^B_{m,n})^2]$$
$$[a^E(m, n)]^2 = \frac{1}{4}[(C^A_{m,n} + S^B_{m,n})^2 + (S^A_{m,n} - C^B_{m,n})^2] \quad \text{(A18)}$$

$$\tan[\phi^W(m, n)] = -(C^B_{m,n} + S^A_{m,n})/(C^A_{m,n} - S^B_{m,n})$$
$$\tan[\phi^E(m, n)] = +(S^A_{m,n} - C^B_{m,n})/(C^A_{m,n} + S^B_{m,n}). \quad \text{(A19)}$$

The one-dimensional power spectra of the time series $c_m(t)$ and $s_m(t)$ (for fixed m) are

$$P_n(c_m) = \frac{1}{2}[(C^A_{m,n})^2 + (C^B_{m,n})^2]$$
$$P_n(s_m) = \frac{1}{2}[(S^A_{m,n})^2 + (S^B_{m,n})^2], \quad \text{(A20)}$$

whereas the one-dimensional real co- and quadrature spectra relating $c_m(t)$ and $s_m(t)$ (for fixed m) are

$$K_n(c_m, s_m) = \frac{1}{2}(C^A_{m,n}S^A_{m,n} + C^B_{m,n}S^B_{m,n})$$
$$Q_n(c_m, s_m) = \frac{1}{2}(C^B_{m,n}S^A_{m,n} - C^A_{m,n}S^B_{m,n}). \quad \text{(A21)}$$

The eastward and westward power spectra defined in Eq. (A7) are given as

$$\mathrm{PW}(m, n) = \frac{1}{4}[P_n(c_m) + P_n(s_m) + 2Q_n(c_m, s_m)]$$
$$\mathrm{PE}(m, n) = \frac{1}{4}[P_n(c_m) + P_n(s_m) - 2Q_n(c_m, s_m)]. \quad \text{(A22)}$$

Averaging over adjacent frequencies and independent samples gives

$$\overline{K_n(c_m, s_m)} = \frac{1}{2}(\overline{C^A_{m,n}S^A_{m,n}} + \overline{C^B_{m,n}S^B_{m,n}})$$
$$\overline{Q_n(c_m, s_m)} = \frac{1}{2}(\overline{C^B_{m,n}S^A_{m,n}} - \overline{C^A_{m,n}S^B_{m,n}}) \quad \text{(A23)}$$

and also

$$\overline{\mathrm{PW}(m, n)} = \frac{1}{4}[\overline{P_n(c_m)} + \overline{P_n(s_m)} + 2\overline{Q_n(c_m, s_m)}]$$
$$\overline{\mathrm{PE}(m, n)} = \frac{1}{4}[\overline{P_n(c_m)} + \overline{P_n(s_m)} - 2\overline{Q_n(c_m, s_m)}]. \quad \text{(A24)}$$

c. Hayashi's theory of standing oscillations

Hayashi (1977) considers the situation in which the fluctuations at a given latitude and level consist only of a single eastward propagating wave, a single westward propagating wave, and a standing oscillation that are all mutually incoherent. In this case it can be shown that the amplitude of the standing oscillation is given by

$$\overline{\mathrm{ST}(m, n)} = \left\{\frac{1}{4}[\overline{P_n(c_m)} - \overline{P_n(s_m)}]^2 + [\overline{K_n(c_m, s_m)}]^2\right\}^{1/2} \quad \text{(A25)}$$

and the "true" eastward and westward propagating waves PE* and PW* are then given by

$$\overline{\mathrm{PE}^*(m, n)} = \overline{\mathrm{PE}(m, n)} - \frac{1}{2}\overline{\mathrm{ST}(m, n)} \quad \text{and} \quad \text{(A26)}$$

$$\overline{\mathrm{PW}^*(m, n)} = \overline{\mathrm{PW}(m, n)} - \frac{1}{2}\overline{\mathrm{ST}(m, n)}. \quad \text{(A27)}$$

Hayashi derives conditions that must hold in order that this approach be at least realizeable. We have checked in our calculations that these conditions do in fact hold.

REFERENCES

Chang, C. P., and H. Lim, 1988: Kelvin wave-CISK: A possible mechanism for the 30–50 day oscillations. *J. Atmos. Sci.,* **45,** 1709–1720.

Frederiksen, J. S., and C. S. Frederiksen, 1997: Mechanisms of the formation of intraseasonal oscillations and Australian monsoon disturbances: The roles of convection, barotropic and baroclinic instability. *Beitr. Phys. Atmos.,* **70,** 39–56.

Gall, R., 1976a: A comparison of linear baroclinic instability theory with the eddy statistics of a general circulation model. *J. Atmos. Sci.,* **33,** 349–373.

——, 1976b: Structural changes of growing baroclinic waves. *J. Atmos. Sci.,* **33,** 374–390.

Hartmann, D. L., 1979: Baroclinic instability of realistic zonal-mean states to planetary waves. *J. Atmos. Sci.,* **36,** 2336–2349.

Hayashi, Y., 1977: On the coherence between progressive and retroregressive waves and a partition of space-time power spectra into standing and traveling parts. *J. Appl. Meteor.,* **16,** 368–373.

Hsu, H.-H., 1996: Global view of the intraseasonal oscillation during northern winter. *J. Climate,* **9,** 2386–2406.

——, B. J. Hoskins, and F.-F. Jin, 1990: The 1985/86 intraseasonal oscillation and the role of the extratropics. *J. Atmos. Sci.,* **47,** 823–839.

Ioannou, P., and R. S. Lindzen, 1986: Baroclinic instability in the presence of barotropic jets. *J. Atmos. Sci.,* **43,** 2999–3014.

Jenkins, G. M., and D. G. Watts, 1968: *Spectral Analysis and its Applications.* Holden-Day, 525 pp.

Julian, P. R., 1975: Comments on the determination of significance levels of the coherence statistics. *J. Atmos. Sci.,* **32,** 836–837.

Kalnay, E., and Coauthors, 1996: The NCEP/NCAR 40-Year Reanalysis Project. *Bull. Amer. Meteor. Soc.,* **77,** 437–472.

Knutson, T. R., and K. M. Weickmann, 1987: 30–60 day atmospheric oscillations: Composite life cycles of convection and circulation anomalies. *Mon. Wea. Rev.,* **115,** 1407–1436.

Lau, K.-M., and T. J. Phillips, 1986: Coherent fluctuations of extratropical geopotential heights and tropical convection in intraseasonal time series. *J. Atmos. Sci.,* **43,** 1164–1181.

Liebmann, B., and D. L. Hartmann, 1984: An observational study of tropical–midlatitude interaction on intraseasonal time scales during winter. *J. Atmos. Sci.,* **41,** 3333–3350.

Lin, J. W., J. D. Neelin, and N. Zeng, 2000: Maintenance of tropical intraseasonal variability: Impact of evaporation–wind feedback and midlatitude storms. *J. Atmos. Sci.,* **57,** 2793–2823.

Lindzen, R. S., 1974: Wave-CISK and tropical spectra. *J. Atmos. Sci.,* **31,** 1447–1449.

——, 1993: Baroclinic neutrality and the tropopause. *J. Atmos. Sci.,* **50,** 1148–1151.

——, D. M. Straus, and B. Katz, 1984: An observational study of large-scale atmospheric Rossby waves during FGGE. *J. Atmos. Sci.,* **41,** 1320–1335.

Madden, R. A., 1979: Observations of large-scale traveling Rossby waves. *Rev. Geophys. Space Phys.,* **17,** 1935–1949.

——, and P. R. Julian, 1971: Description of a 40–50 day oscillation in the zonal wind in the tropical Pacific. *J. Atmos. Sci.,* **28,** 702–708.

——, and ——, 1994: Observations of the 40–50-day tropical oscillation—A review. *Mon. Wea. Rev.,* **122,** 814–837.

Mechoso, C. R., and D. L. Hartmann, 1982: An observational study of traveling planetary waves in the Southern Hemisphere. *J. Atmos Sci.,* **39,** 1921–1935.

Miller, R., and R. S. Lindzen, 1992: Organization of rainfall by an unstable jet with application to African waves. *J. Atmos. Sci.,* **49,** 1523–1540.

Pedlosky, J., 1987: *Geophysical Fluid Dynamics.* 2d ed. Springer, 710 pp.

Pratt, R. W., 1976: The interpretation of space-time spectral quantities. *J. Atmos. Sci.,* **33,** 1060–1066.

Salby, M. L., 1981a: Rossby normal modes in nonuniform background configurations. Part I: Simple fields. *J. Atmos. Sci.,* **38,** 1803–1826.

——, 1981b: Rossby normal modes in nonuniform background configurations. Part II: Equinox and solstice conditions. *J. Atmos. Sci.,* **38,** 1827–1840.

Schubert, S. D., and C.-K. Park, 1991: Low-frequency intraseasonal tropical–extratropical interactions. *J. Atmos. Sci.,* **48,** 629–650.

Simmons, A. J., and B. J. Hoskins, 1978: The life cycles of some nonlinear baroclinic waves. *J. Atmos. Sci.,* **35,** 414–432.

Stevens, D., and R. S. Lindzen, 1978: Tropical wave-CISK with a moisture budget and cumulus friction. *J. Atmos. Sci.,* **35,** 940–961.

Straus, D. M., 1981: Long-wave baroclinic instability in the troposphere and stratosphere with spherical geometry. *J. Atmos. Sci.,* **38,** 409–426.

——, and J. Shukla, 1981: Space-time spectral analysis of a GLAS general circulation model and a comparison with observations. *J. Atmos. Sci.,* **38,** 902–917.

——, R. S. Lindzen, and A. M. DaSilva, 1987: The characteristic Rossby frequency. *J. Atmos. Sci.,* **44,** 1100–1105.